

Promoting exsolution of RuFe alloy nanoparticles on $\text{Sr}_2\text{Fe}_{1.4}\text{Ru}_{0.1}\text{Mo}_{0.5}\text{O}_{6-\delta}$ via repeated redox manipulations for CO_2 electrolysis

Houfu Lv^{1,2,5}, Le Lin^{1,3,5}, Xiaomin Zhang¹, Rongtan Li ^{1,2}, Yuefeng Song¹, Hiroaki Matsumoto⁴, Na Ta¹, Chaobin Zeng⁴, Qiang Fu ¹, Guoxiong Wang ¹✉ & Xinhe Bao¹

Metal nanoparticles anchored on perovskite through in situ exsolution under reducing atmosphere provide catalytically active metal/oxide interfaces for CO_2 electrolysis in solid oxide electrolysis cell. However, there are critical challenges to obtain abundant metal/oxide interfaces due to the sluggish diffusion process of dopant cations inside the bulk perovskite. Herein, we propose a strategy to promote exsolution of RuFe alloy nanoparticles on $\text{Sr}_2\text{Fe}_{1.4}\text{Ru}_{0.1}\text{Mo}_{0.5}\text{O}_{6-\delta}$ perovskite by enriching the active Ru underneath the perovskite surface via repeated redox manipulations. In situ scanning transmission electron microscopy demonstrates the dynamic structure evolution of $\text{Sr}_2\text{Fe}_{1.4}\text{Ru}_{0.1}\text{Mo}_{0.5}\text{O}_{6-\delta}$ perovskite under reducing and oxidizing atmosphere, as well as the facilitated CO_2 adsorption at RuFe@ $\text{Sr}_2\text{Fe}_{1.4}\text{Ru}_{0.1}\text{Mo}_{0.5}\text{O}_{6-\delta}$ interfaces. Solid oxide electrolysis cell with RuFe@ $\text{Sr}_2\text{Fe}_{1.4}\text{Ru}_{0.1}\text{Mo}_{0.5}\text{O}_{6-\delta}$ interfaces shows over 74.6% enhancement in current density of CO_2 electrolysis compared to that with $\text{Sr}_2\text{Fe}_{1.4}\text{Ru}_{0.1}\text{Mo}_{0.5}\text{O}_{6-\delta}$ counterpart as well as impressive stability for 1000 h at 1.2 V and 800 °C.

¹State Key Laboratory of Catalysis, Dalian National Laboratory for Clean Energy, Dalian Institute of Chemical Physics, Chinese Academy of Sciences, Dalian, P. R. China. ²University of Chinese Academy of Sciences, Beijing, P. R. China. ³School of Physical Science and Technology, ShanghaiTech University, Shanghai, P. R. China. ⁴Hitachi High-tech (Shanghai) Co., Ltd, Shanghai, P. R. China. ⁵These authors contributed equally: Houfu Lv, Le Lin. ✉email: wanggx@dicp.ac.cn

Solid oxide electrolysis cell (SOEC) for CO₂ electrolysis can efficiently convert renewable electricity into chemical energy as stored in CO¹⁻⁴. Perovskite and its derivatives have been investigated as one of the most promising SOEC cathode materials due to their considerable catalytic activity and stability⁵. Redox exsolution on perovskite is a feasible strategy to manipulate catalytic active sites, in which catalytically active transition metals such as Rh, Pd, Pt, Fe, Ni, Co, etc. are substituted in the perovskite lattice as solid solution under an oxidizing atmosphere, and then exsolved as metal nanoparticles (NPs) anchored on the perovskite surface under reducing atmosphere⁶⁻¹⁰. The perovskites undergoing redox exsolution exhibit unique catalytic activity, thermal stability, and coking resistance in SOEC, solid oxide fuel cell (SOFC), and other heterogeneous catalytic reactions¹¹⁻¹⁶.

The perovskite used in SOEC and SOFC has a large crystalline size of several hundred nanometers due to high-temperature (>1000 °C) calcination during powder preparation and cell fabrication^{17,18}. The exsolution process occurs initially within the bulk perovskite with uniformly doped active metal cations^{19,20}, and only a limited proportion of metal NPs can be exsolved onto the perovskite surface under reducing atmosphere due to the sluggish diffusion process of dopant B-site cations inside the perovskite lattice^{17,21-23}. Several strategies have been developed to promote the exsolution of metal NPs such as A-site defect^{18,24,25}, phase transformation engineering^{26,27}, and topotactic ion exchange^{28,29}, etc. These strategies indeed facilitate the exsolution process, however, the critical issue of long diffusion distance remains unresolved. Ideal exsolution may necessitate the enrichment of the dopant B-site cations underneath the perovskite surface, which would facilitate the exsolution on the surface without the need of diffusion from the bulk^{21,30}. Therefore, developing a reliable strategy for surface engineering regulation would provide more viable options for promoting the in situ growth of highly active and stable metal/oxide interfaces.

Herein, we propose a strategy to promote the exsolution of RuFe alloy NPs on Sr₂Fe_{1.4}Ru_{0.1}Mo_{0.5}O_{6-δ} (SFRuM) perovskite by enriching the active Ru underneath the surface via repeated redox manipulations. The atomic-scale dynamic structure evolution of SFRuM perovskite under the reducing and oxidizing atmosphere is investigated using in situ scanning transmission electron microscopy (STEM) with energy-dispersive X-ray spectroscopy (EDS) and electron energy loss spectrum (EELS), in combination with in situ X-ray diffraction (XRD) and density functional theory (DFT) calculations. Under reducing atmosphere, Ru atoms in SFRuM are preferentially exsolved to form Ru NPs anchored on the SFRuM surface, and then Fe atoms migrate onto the surface of Ru NPs to generate RuFe intermetallic alloy. Under oxidizing atmosphere, Fe atoms in RuFe alloy are preferentially oxidized and move back to the perovskite, and subsequently, Ru atoms migrate back to surface-biased B-sites. Fe species can reversibly serve as a “templating agent” drawing Ru atoms out of the perovskite. The repeated redox manipulations result in the enrichment of Ru underneath the SFRuM perovskite surface and thus facilitate abundant exsolution of RuFe alloy NPs under reducing atmosphere. The density of exsolved RuFe alloy NPs reaches ~21,000 particles μm⁻² after four redox manipulations, which is ~3.6 times as much as that after the first reduction treatment while the size of RuFe alloy NPs maintains similar. The in situ grown RuFe@SFRuM interfaces facilitate CO₂ adsorption and boost CO₂ electrolysis performance in SOEC with impressive stability for 1000 h.

Results

In situ STEM and crystalline structure characterization. The crystalline structures of the as-prepared, reduced, reoxidized, and re-reduced SFRuM were examined using XRD and transmission

electron microscopy (TEM) (Supplementary Fig. 1). As-prepared SFRuM shows a double perovskite structure. The reduced sample presents a mixture of the Ruddlesden-Popper layered perovskite (RP-SFRuM) with RuFe alloy phase (SFRuM R1 and RuFe@SFRuM), indicating that the phase transition and exsolution of RuFe alloy occurs during the reduction process. The crystalline structure reconstructs to the initial state after reoxidation (SFRuM O1), and RuFe alloy could be exsolved again after re-reduction (SFRuM R2), which shows a characteristic self-regeneration function^{11,12,31}.

Using in situ aberration-corrected STEM with a secondary electron detector, we are able to conduct surface morphology evolution during redox manipulations. The perovskite initially exhibited a pristine surface with no existence of exsolved metal NPs after reduction at 600 °C (Supplementary Fig. 2b). A few small-size metal NPs emerged until the reduction temperature reached 800 °C (Fig. 1a), which were apparently present on the surface after continuous reduction for ~30 min (Fig. 1b). Under oxidizing atmosphere, metal NPs were oxidized with a large size and then redissolved into the perovskite completely (Fig. 1c, d and Supplementary Fig. 2). In situ STEM results confirm that Ru in SFRuM repeats the cycle of forming a solid solution and segregation as metal NPs during redox manipulations. Subsequently, SFRuM O1 was also investigated under reducing atmosphere by in situ STEM and different phenomena were observed, in which metal NPs could be exsolved after reduction at 600 °C (Fig. 1e and Supplementary Fig. 3). Abundant metal NPs were present on the surface after increasing the reduction temperature to 800 °C (Fig. 1f-h), and the NPs can be observed mainly on the steps of the perovskite, where the presence of crystallographic defects can act as nucleation sites^{18,20} (Supplementary Fig. 3i-k). Metal NPs were easier to be exsolved on SFRuM O1, corroborating different segregation properties associated with the variation in surface composition.

To provide insight into the difference in exsolution, the correlation between the redox manipulations and the number of exsolved metal NPs was investigated (Fig. 1i-l and Supplementary Fig. 4). In the case of the SFRuM R1, a limited fraction of B-site cations could be exsolved (Fig. 1i). In contrast, much more exsolved metal NPs were observed on redox manipulated samples (Fig. 1j, k and Supplementary Fig. 4). The relationship between the density of the exsolved metal NPs and the number of the redox cycles is shown in Fig. 1l, and the density of exsolved metal NPs increases with the number of redox cycles. The density of exsolved metal NPs reaches ~21,000 particles μm⁻² after four redox manipulations, which is ~3.6 times as much as that of SFRuM R1. Notably, the redox manipulations do not affect the Fe/Ru ratio and the size of the exsolved metal NPs (Fig. 1l and Supplementary Fig. 5). In consequence, exsolution is greatly promoted through repeated redox manipulations, which is probably due to Ru enrichment underneath the SFRuM surface.

To investigate the crystalline structure and composition of the perovskite after reduction (SFRuM R1) and after reoxidation (SFRuM O1), we examined the samples using atomic-scale STEM and STEM-EDS elemental maps. As shown in the high angle annular dark field (HAADF)-STEM image of SFRuM R1 (Fig. 2a), metal NPs were exsolved from the parent perovskite. Atomic-scale STEM-EDS elemental maps were conducted in the parent perovskite with and without metal NPs to investigate the ordering and positions of Ru (Fig. 2b, c and Supplementary Fig. 6). Ru signals were not clearly observed in the perovskite except in the metal NPs (Fig. 2c), suggesting that part of the Ru was exsolved into the metal NPs (Fig. 2b). Meanwhile, Ru signals were clearly observed in the positions of Fe and Mo for SFRuM O1, which implies the complete dissolution of Ru into the B-sites of perovskite after reoxidation (Fig. 2d and Supplementary Fig. 7).

The dynamic evolution upon exsolution and dissolution of RuFe alloy NPs was investigated by in situ STEM to reveal the

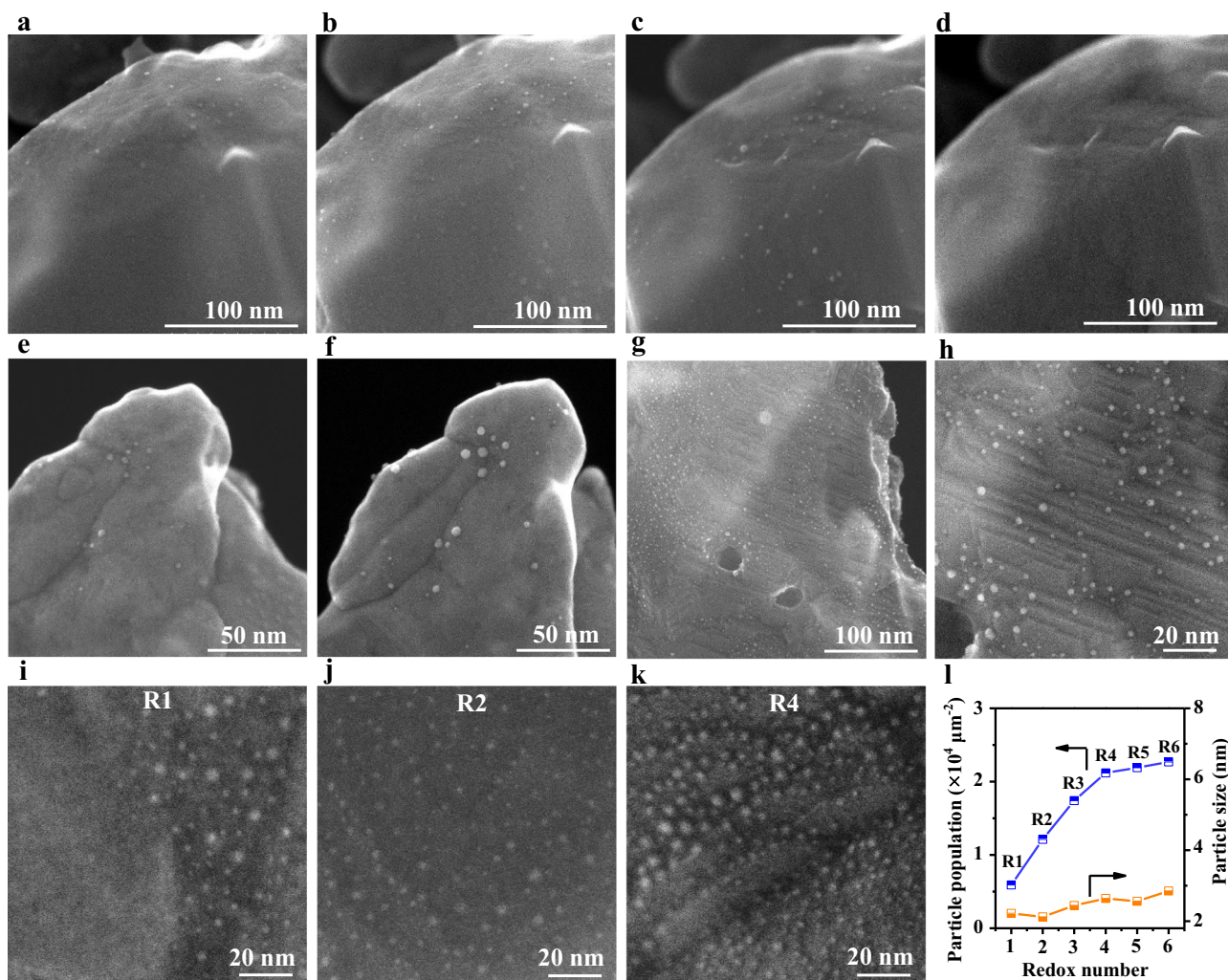


Fig. 1 Morphological study of the SFRuM catalysts. In situ secondary electron (SE)-STEM images of SFRuM after reduction at 800 °C for -15 min (a), after reduction at 800 °C for -30 min (b), after reoxidation at 800 °C for -30 min (c), and after reoxidation at 800 °C for -40 min (d). In situ SE-STEM images of SFRuM O1 after reduction at 600 °C for -10 min (e), after reduction at 800 °C for -10 min (f), and after reduction at 800 °C for -60 min (g). h Magnified image of (g). Ex situ SE-STEM images of SFRuM R1 (i), SFRuM R2 (j), and SFRuM R4 (k). l Population and size distribution of metal NPs exsolved after different redox manipulations.

mechanism underlying the surface enrichment of Ru. In situ dark field (DF)-STEM images and STEM-EDS elemental maps were collected during the reduction process, and Ru-rich metal NPs were exsolved at the preliminary stage at 800 °C (Fig. 2e, f and Supplementary Fig. 8a). During the assembling process of RuFe alloy NPs, reduced Fe was observed to migrate onto the surface of Ru NPs through the Ru@SFRuM interface (Fig. 2g and Supplementary Figs. 8,14), which is similar to the formation process of strong metal-support interaction³². The transient overlayer structure is the intermediate state, and RuFe alloy NPs could be assembled after reduction at 800 °C for ~60 min and then at 850 °C for ~30 min (Fig. 2j, n and Supplementary Fig. 9), which was also validated by ex situ EDS results (Supplementary Figs. 10,11). In addition, epitaxially oriented metal NPs evolution remains isotropic, growing proportionally in both height and width simultaneously³³ (Fig. 2h, i and Supplementary Figs. 12, 13), especially during the migration of Fe onto the Ru NPs (Supplementary Fig. 14).

The evolution of RuFe alloy NPs under an oxidation atmosphere was also investigated (Supplementary Fig. 15). As illustrated by the in situ DF-STEM, STEM-EDS, and STEM-EELS results in Fig. 2j, n, p, metallic Ru and Fe were uniformly

distributed in the exsolved metal NPs, demonstrating the formation of a RuFe alloy phase. A structure of FeO_x shell and RuFe alloy core was well reflected after in situ reoxidation in 10 Pa of O₂ at 200 °C for ~70 s (Fig. 2k, o, q, Supplementary Fig. 9 and Supplementary Movie 1), in line with ex situ STEM-EDS results (Supplementary Figs. 10, 16, 17). After exposure to the O₂ atmosphere at 800 °C for 30 min, the metal NPs evolved into a regular shape (Fig. 2l and Supplementary Figs. 18, 19). Changes in the constituent of RuFe metal NPs into Ru-rich metal NPs could be ascribed to the prior oxidation and dissolution of FeO_x into the perovskite (Fig. 2q). As a manifestation of the self-regeneration function, the Ru-rich metal NPs dissolved into the perovskite completely after exposure to the O₂ atmosphere for 60 min at 800 °C (Fig. 2m and Supplementary Figs. 15, 19). In situ STEM, STEM-EDS, and STEM-EELS results demonstrate the priority exsolution but the hysteresis dissolution of Ru in RuFe alloy NPs, which reveals the formation mechanism of Ru enrichment underneath the SFRuM surface.

Crystal structure evolution and DFT calculations. In situ XRD experiments were carried out to monitor the structural evolution

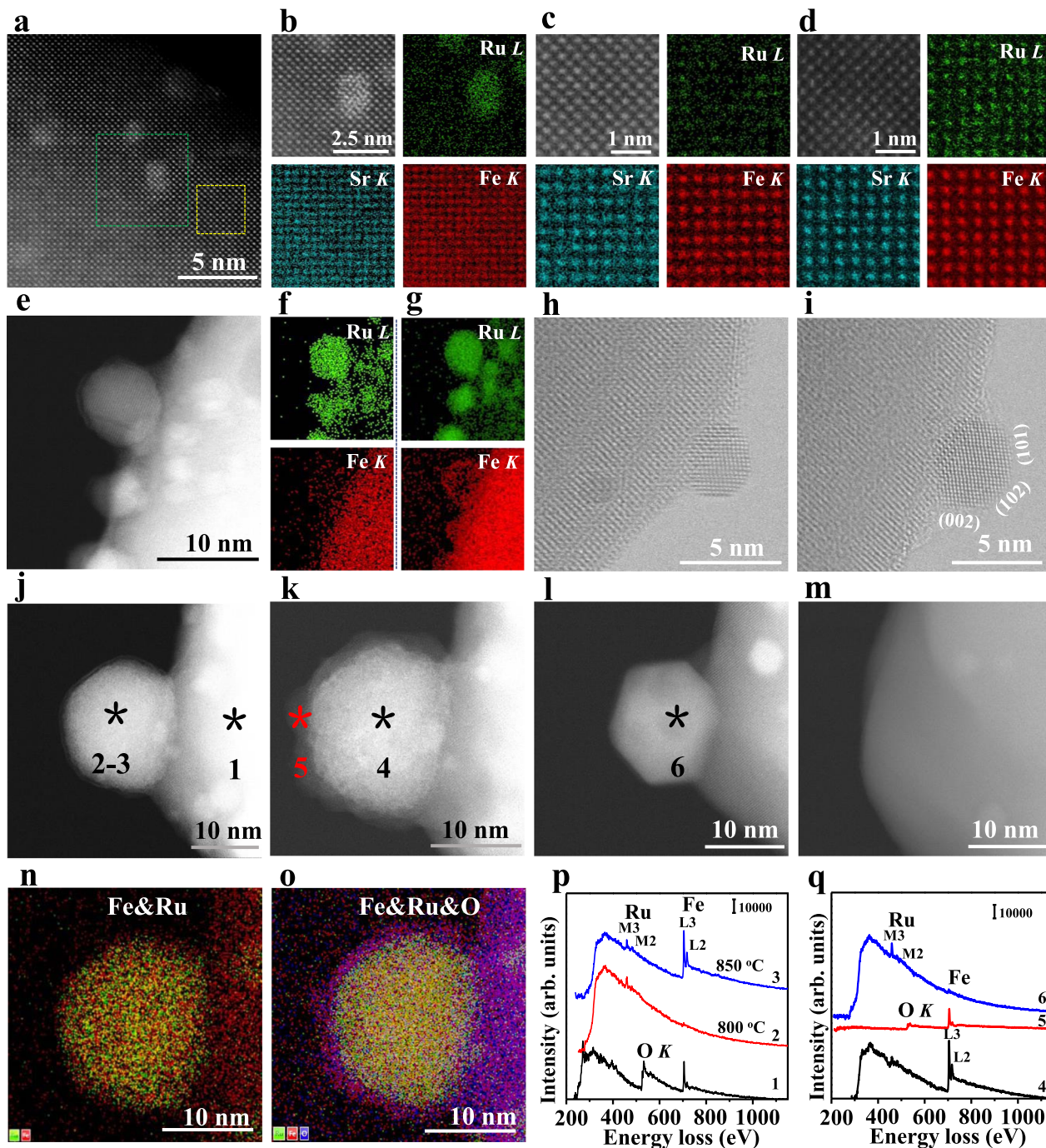


Fig. 2 In situ STEM, STEM-EDS, and STEM-EELS results. **a** HAADF-STEM image of SFRuM R1 and the atomic-scale elemental maps, circled with a green dotted line **b** and a yellow dotted line **c** (010). **d** HAADF-STEM image of SFRuM O1 and the atomic-scale elemental maps (010). **e** In situ DF-STEM image and STEM-EDS elemental maps of SFRuM at 800 °C for -15 min (**f**) and then at 850 °C for -15 min (**g**). In situ BF-STEM images after reduction at 800 °C for -15 min (**h**) and then at 850 °C for -15 min (**i**). In situ DF-STEM images of SFRuM after reduction at 800 °C for -60 min and 850 °C for -30 min (**j**), after reoxidation at 200 °C for -70 s (**k**), after reoxidation at 800 °C for -30 min (**l**), and after reoxidation at 800 °C for -60 min (**m**). **n, o** The STEM-EDS elemental maps of **j** and **k**. **p, q** In situ STEM-EELS spectra in **j-l**.

during redox manipulations at 800 °C (Fig. 3a, b). Layered perovskite with RuFe alloy phases emerged during reduction and vanished during reoxidation. With increasing reduction time in the first reduction step, a weak phase transformation and RuFe alloy phase emerged, and the mixed structure evolved back to the original perovskite form after reoxidation. Similar observations were acquired during the second redox cycle, except that the characteristic peak intensity of SFRuM was weakened, whereas the characteristic peak intensity of emergent RP phase perovskite

and RuFe alloy was enhanced (Fig. 3a, b). This phenomenon is consistent with the behaviors observed in situ (Fig. 1e–h) and ex situ (Fig. 1i–k and Supplementary Fig. 4) SE-STEM results that promoted exsolution was triggered for the reoxidized SFRuM. SFRuM shows unexpected but reasonable redox self-regeneration functions, which is due to surface enrichment of Ru as mentioned above.

The changes in chemical states and components of surface-biased elements were demonstrated by X-ray photoemission

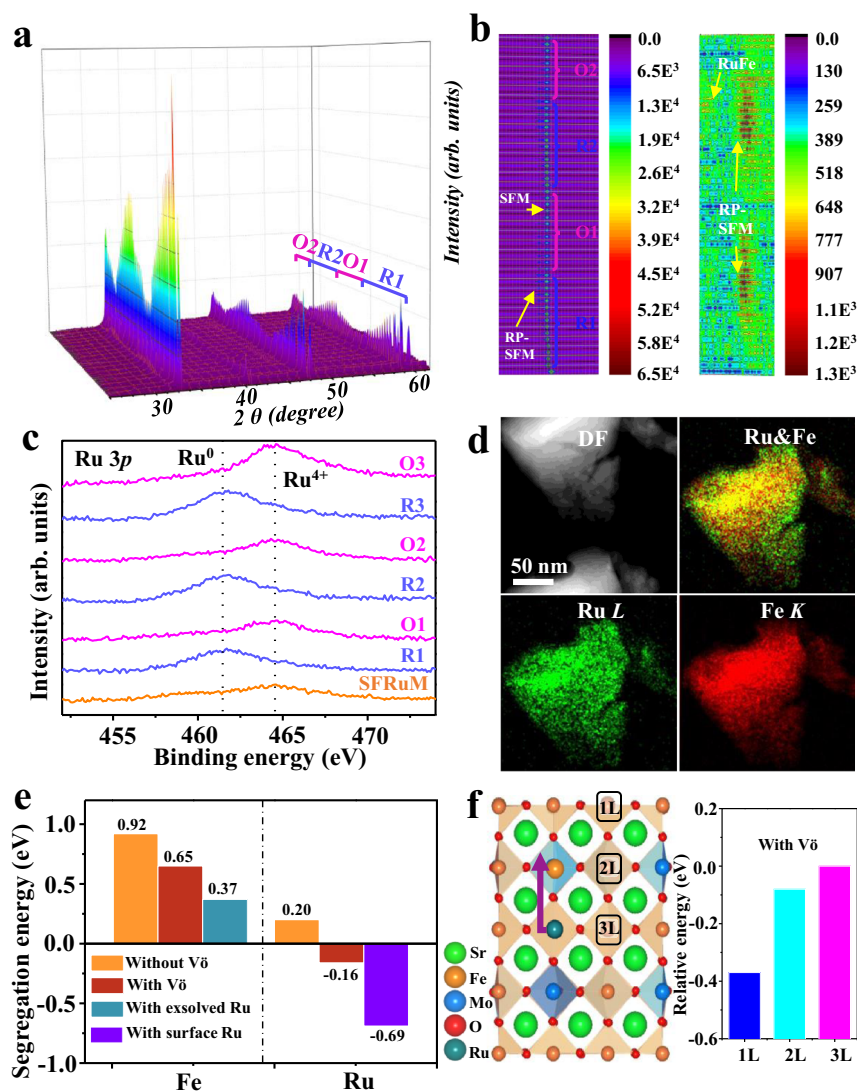


Fig. 3 Characterization and DFT results of SFRuM. **a** In situ XRD patterns of as-prepared SFRuM upon switching between reducing and oxidizing atmosphere at 800 °C. **b** Depth profile of XRD patterns at 31–33° and 43–45° of (a). **c** Ru 3p XPS spectra of SFRuM after redox manipulations. **d** STEM-EDS elemental maps of SFRuM O3. **e** Comparison of segregation and co-segregation energies with Fe and the doped Ru. **f** Schematic of exsolution process with relative energy of the slab as a function of Ru positions. 1L denotes the surface layer and 3L corresponds the inner layer.

spectroscopy (XPS) analysis. Note that the C 1s and Ru 3d photoemissions overlap, hence Ru 3p photoemissions were collected. Peak intensity of Ru⁴⁺ in the as-prepared SFRuM with the binding energy of 464.2 eV is relatively weak³⁴, while metallic Ru⁰ species with the binding energies of 461.3 eV can be observed for SFRuM R1 with high intensity. After reoxidation (SFRuM O1), the same chemical environment with SFRuM demonstrates redox recyclability and the enhanced intensity of Ru 3p_{3/2} spectrum displays an increase of Ru amount on the perovskite surface of SFRuM O1³⁴. According to the semiquantitative XPS analysis, a significant increase in the atomic Ru/Sr ratio from 0.053 to 0.12 can be observed after three redox manipulations (Fig. 3c and Supplementary Table 1), indicative of gradual enrichment of Ru amount on the surface via redox manipulations. To gain direct insights into the compositional change, we performed STEM-EDS analysis. The representative elemental maps clearly show a homogeneous distribution of Ru in SFRuM, whereas SFRuM O3 substantiates the formation of a core-shell structure, demonstrating the formation of Ru-enriched surface through microcosmic elemental segregation (Fig. 3d and Supplementary

Figs. 20, 21), which confirms the self-enrichment function of SFRuM after repeated redox manipulations.

The sequential exsolution of Ru and Fe and surface enrichment of Ru are further elaborated by DFT calculations¹⁴ (Fig. 3e, f and Supplementary Fig. 22). The calculated co-segregation energies of Ru and Fe with oxygen vacancy (V_O) are -0.16 and 0.65 eV, respectively, which are lower than those without V_O, indicative of the critical role of V_O in the exsolution^{22,25,30}. The lower segregation energy illustrates that Ru has a higher tendency to be exsolved than Fe. Ru exsolution to the surface could decrease the segregation energy of Fe to 0.37 eV and thus facilitates Fe exsolution to form RuFe alloy³⁵, which is in good agreement with the in situ STEM-EDS results (Fig. 2f, g). Figure 3f displays the calculated total energies of SFRuM slabs with surface-segregated and solid-solution states of Ru atoms. The surface-segregated state is slightly more stable than the solid-solution one. Therefore, the exsolution may originate from the preferential migration of Ru to form Ru metal NPs^{28,29}. Subsequently, Fe atoms migrate to the Ru metal NPs to form RuFe alloy NPs (Fig. 2g, j). Upon subsequent exposure to the O₂ atmosphere, Fe moves back to the

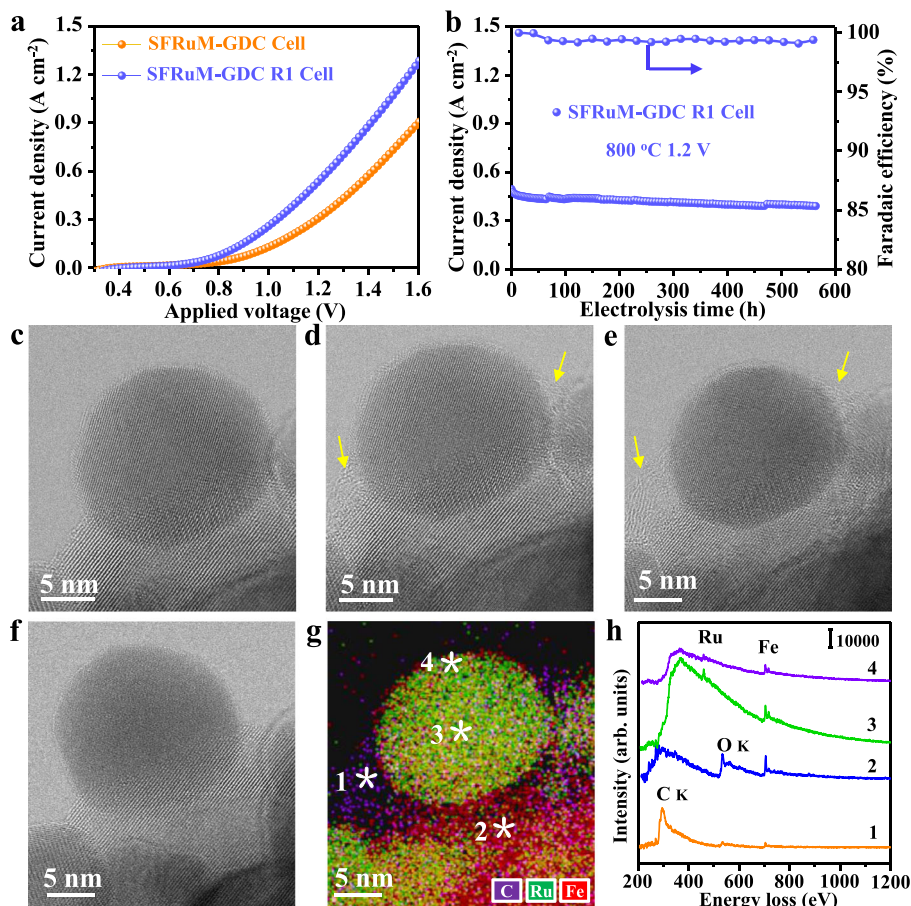


Fig. 4 CO_2 electrolysis and in situ STEM results. **a** I–V curves of SFRuM-GDC and SFRuM-GDC R1 cells at 800 °C. **b** Stability test of SFRuM-GDC R1 cell and CO Faradaic efficiencies at 800 °C and 1.2 V. In situ BF-STEM images of SFRuM after in situ reduction at 800 °C for -1 h (**c**), after exposed to 10 Pa of CO_2 for 10 min at 200 °C (**d**), after exposed to 10 Pa of CO_2 for 30 min at 200 °C (**e**) (The adsorbed species are indicated by yellow arrows), and after heating up to 800 °C under vacuum (**f**). **g**, **h** In situ STEM-EDS map and in situ STEM-EELS spectra of (**e**).

bulk perovskite preferentially, and subsequently Ru migrates back to the surface-biased B-sites. Ru is pulled out from perovskite bulk gradually through such a cyclic process and consequently forms a Ru-enriched surface on the perovskite. After surface enrichment of Ru, the co-segregation energy of Ru with V_O could be further reduced to -0.69 eV, and thus promotes the exsolution of more RuFe alloy NPs (Fig. 3e), consistent with in situ (Fig. 1e–h) and ex situ (Fig. 1i–k and Supplementary Fig. 4) SE-STEM results. Redox manipulations would result in enrichment of dopant Ru cations underneath the perovskite surface, which is conducive to promote the exsolution of RuFe alloy NPs.

Electrochemical performance. Figure 4a and Supplementary Fig. 23 show CO_2 electrolysis performance using $\text{La}_{0.8}\text{Sr}_{0.2}\text{Ga}_{0.8}\text{Mg}_{0.2}\text{O}_{3-\delta}$ (LSGM) electrolyte supported electrolysis cell. SFRuM perovskite phase and $\text{Gd}_{0.2}\text{Ce}_{0.8}\text{O}_{1.9}$ (GDC) fluorite phase were used as the composite cathode (SFRuM-GDC). As-prepared SFRuM-GDC cell exhibited relatively low current density as Ru is less exposed onto the surface. High CO_2 electrolysis performance can be achieved for the SFRuM-GDC R1 cell, with a few active RuFe alloy NPs exsolved on the surface (Fig. 1i). The stability of the SFRuM-GDC R1 cell for CO_2 electrolysis was examined at 800 °C and 1.2 V (Fig. 4b). There was a slight drop in the primary stage and the current density showed no observable degradation for 567 h. No coking was confirmed by the calculated CO Faradaic efficiencies (Fig. 4b) and Raman results (Supplementary Fig. 24). Conventionally, these anchored metal NPs with

preferential orientations towards the perovskite support will maintain the active interfaces under reaction conditions (Supplementary Figs. 13, 16)^{36–39}. The current density of 2.25 A cm^{-2} was obtained using a thin LSGM electrolyte that exceeds most state-of-the-art electrolyzers (Supplementary Fig. 25 and Table 2), benefiting from the highly active metal-perovskite interfaces^{40,41}.

To directly observe and obtain more detailed information, we conducted in situ STEM on the dynamic evolution of the RuFe@SFRuM interface under the CO_2 atmosphere. A stable and clean RuFe@SFRuM interface could be obtained after in situ reduction at 800 °C (Fig. 4c and Supplementary Fig. 26). Upon exposure to CO_2 atmosphere at 200 °C, a gradual decoration of the interface with an amorphous material of low-contrast was observed (yellow arrow in Fig. 4d, e, Supplementary Figs. 27, 28, and Supplementary Movie 2). STEM-EDS elemental maps and STEM-EELS spectra (Fig. 4g, h) reveal that these species contain carbon and oxygen, which are more abundant than that on the surface of RuFe alloy NPs and the parent perovskite. These results indicate that RuFe@SFRuM interfaces facilitate CO_2 adsorption compared to either RuFe alloy NPs or parent perovskite alone. After heating up to 800 °C under vacuum, adsorbed species disappear probably through CO or CO_2 desorption (Fig. 4f). The in situ approach enables to derive a holistic view under the reaction conditions that is important for the understanding of the RuFe@SFRuM interface characteristics.

Ru-containing SFRuM perovskite catalyst can function as a self-regeneration and surface Ru enrichment catalyst via redox

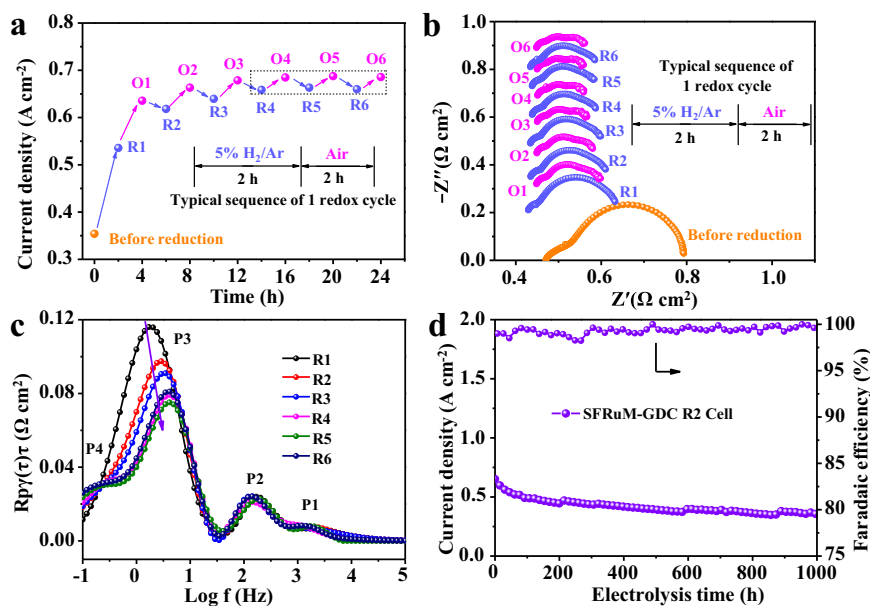


Fig. 5 Electrochemical results. **a** CO₂ electrolysis performance of SFRuM-GDC cell after six redox cycles at 800 °C and 1.2 V. **b** The corresponding in situ EIS results. **c** DRT spectra of the RuFe alloy NPs decorated cells calculated from **b**. **d** Stability test of SFRuM-GDC R2 cell and CO Faradaic efficiencies at 800 °C and 1.2 V.

manipulations. The electrochemical performance of the preceding SFRuM after every redox manipulation was subsequently assessed for CO₂ electrolysis. The measurement was carried out sequentially over six repetitions of redox cycles. CO₂ electrolysis performance was improved after the first reduction treatment, known as the decoration of RuFe alloy NPs. Performance improvement can be further obtained for SFRuM-GDC O1 cell, mainly due to the atomically dispersed lattice confined Ru sites^{34,42}. The population of the exsolved RuFe alloy NPs increases with the cycle of redox manipulations due to the surface enrichment of Ru (Fig. 11), which resulted in a gradual enhancement of CO₂ electrolysis performance. Compared to SFRuM-GDC cell, the enhancement in current density for CO₂ electrolysis is 51.3% for SFRuM-GDC R1 cell, 74.6% for SFRuM-GDC R2 cell, and finally reaches 86.4% for SFRuM-GDC R6 cell at 800 °C and 1.2 V (Fig. 5a). The current density was improved during every reduction process until after four redox manipulations, and then could be reproducible on/off on a regular basis^{43,44} (Fig. 5a), clearly revealing the structure-activity relationship. The surface characteristics were greatly changed with the surface enrichment of Ru via redox manipulations, promoting the exsolution of abundant RuFe alloy NPs and facilitating the CO₂ electrolysis.

Electrochemical impedance spectroscopy (EIS) can provide operando insights into the switching of active sites for CO₂ electrolysis in both reducing and oxidizing atmospheres (Fig. 5b). The high-frequency intercept of EIS with the real axis represents the ohmic resistance (R_o) mainly from the electrolyte, and the distance between the highest and lowest frequency intercepts of EIS with the real axis are related to the electrode polarization resistance (R_p). Periodic diminution of R_o demonstrates the enhanced conductivity, which can be attributed to the synergistic effect of the exsolved metal NPs, the RP phase perovskite through a phase transition, and the increased oxygen vacancies during the exsolution⁴⁵. And the variation tendency of the total resistance corresponds to the CO₂ electrolysis performance in Fig. 5a. The EIS can separate into several elementary electrode processes through distribution function of relaxation times (DRT, Supplementary Figs. 29, 30) analysis, including ion migration process

(P1), oxygen evolution reaction at the anode (P2), electrochemical adsorption and activation process (P3), and gas diffusion process (P4) from high to low frequency range^{46–48}. Generally, the resistance of the P3 process dominates CO₂ electrolysis kinetics^{31,49}, which strongly depends on the catalytic active sites. The decreasing peak area of the P3 process after reduction and re-reduction processes takes responsibility for the gradually enhanced CO₂ electrolysis performance (Fig. 5a, c), which is an essential manifestation of gradually promoted exsolution of RuFe alloy NPs. Compared with those of other perovskite electrodes, SFRuM shows the lowest polarization resistance of 0.11 $\Omega \text{ cm}^{-2}$ at 800 °C and 1.2 V under similar test conditions (Supplementary Table 3), revealing a great improvement in the catalytic activity through redox manipulations. In addition, the stability of the exsolved NPs obtained via redox manipulations was evaluated for SFRuM-GDC R2 cell (Fig. 5d), and the CO₂ electrolysis performance remained relatively stable for 1000 h, validating the impressive activity, stability, and renewability of the metal/oxide interface (Supplementary Fig. 31). In situ redox manipulations to regenerate catalysts and promote the exsolution of abundant metal NPs are crucial for the perovskite-based catalysts, which could serve as a general strategy for other exsolution systems.

Theoretical simulation. DFT calculations provide insights into the essence of reactivity differences (see “Methods” and Supplementary Figs. 32–34 for details). CO₂ activation and oxygen migration are the key issues to be taken into account. We focus on the CO₂ activation process as SFM and RP-SFM perovskites possess similar O²⁻ migration ability³¹. The CO₂ activation process involves three elementary steps: CO₂ adsorption (ΔG_1), dissociation (ΔG_2), and CO desorption (ΔG_3). As shown in Fig. 6a, ΔG_1 is 0.72 eV on the Fe site of SFRuM surface (Fe-SFRuM), which is -0.26 eV at the Fe-terminated interface (RuFe@SFRuM) through a bidentate-CO₂* formation with the C-Fe bonding and O (of CO₂) trapping at the V_O (Fig. 6b)⁵⁰. These CO₂* species subsequently dissociate to CO* through an electrochemical process with $2e^-$ transfer⁴⁷. For the third

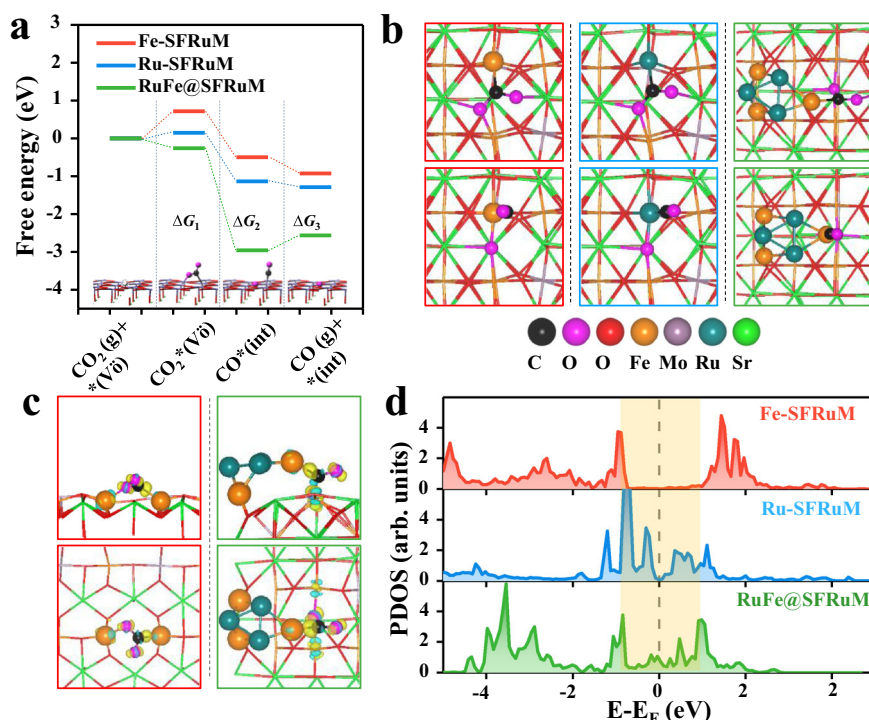


Fig. 6 DFT-based energetic and electronic structure analysis of CO_2 electrolysis. **a** Gibbs free energy diagram for CO_2 electrolysis over three active sites: Fe and Ru centers at SFRuM (121) surface and Fe border at RuFe@SFRuM interface (800 °C and -1.0 V). $*(\text{V}_0)$ and $*(\text{int})$ denote the oxygen-defected and the intact surfaces. **b** Corresponding local atomic configurations (top view) from CO_2^* (upper) to CO^* (lower). **c** Top (upper) and side (lower) views of electron density differences of CO_2 adsorption over Fe-SFRuM surface and RuFe@SFRuM interface. Yellow and cyan areas denote the accumulation and dissipation of electrons. **d** PDOS of active Fe and Ru centers at SFRuM surface and RuFe@SFRuM interface before CO_2 adsorption. The dashed gray line marks the Fermi level and the orange block highlights the main difference of the d -band.

elementary step, CO^* desorption energies (ΔG_3) are -0.43 and 0.39 eV for Fe-SFRuM and RuFe@SFRuM, respectively. The rate-determining step is CO_2 adsorption ($\Delta G_1 = 0.72$ eV) for Fe-SFRuM and CO desorption ($\Delta G_3 = 0.39$ eV) for RuFe@SFRuM, therefore, the latter is relatively favorable and represents a high activity. Figure 6c shows that electron transfer mainly occurs between C and Fe, indicative of a pivotal role of Fe in CO_2 electrolysis. In the light of projected density of states (PDOS) (Fig. 6d), Fe at RuFe@SFRuM interface possesses richer densities (the orange block highlights) around the Fermi level and a higher d -band center ($\epsilon_d = -1.58$) compared to SFRuM surface ($\epsilon_d = -1.76$), indicative of strong bonding of the metal/oxide interface to CO_2 . We also note that the interface can provide a highly O-constrained V_0 (estimated by the V_0 formation energy, $E_{\text{ovf}} = -1.14$ eV) as compared to the surface ($E_{\text{ovf}} = 0.36$ eV). Therefore, we suggest that the RuFe@SFRuM interface boosts the CO_2 electrolysis, benefiting from the synergetic effect of the interface confined Fe and the unique oxygen vacancy. Additionally, Fe-terminated (RuFe@SFRuM) and Ru-terminated (FeRu@SFRuM) interface models exhibit a significantly different adsorbability for CO , implying interface termination engineering is also a strategy targeted for tuning the performance (Supplementary Fig. 35).

With regard to the surface-enrichment effect of Ru, the comparison is made between the isolated Ru site on the SFRuM surface (Ru-SFRuM) and the pristine Fe-SFRuM. CO_2 electrolysis should mainly lie at the electronic effect owing to the difference between $3d$ -block Fe and $4d$ -block Ru⁵¹. In Fig. 6a, CO_2 adsorption on Ru-SFRuM is enhanced by 0.57 eV relative to that on Fe-SFRuM, indicating that CO_2 is well activated by the isolated Ru site. Further PDOS analysis in Fig. 6d shows that the isolated Ru exhibits more enriched d -band states around the Fermi level than

Fe, causing an intensified interaction between Ru and CO_2 . Such distinctive electronic structure of Ru-SFRuM improves the activity of CO_2 electrolysis versus that of Fe-SFRuM, which is consistent with the improved CO_2 electrolysis performance by surface enriched Ru in Fig. 5a. Periodic oscillation in CO_2 electrolysis performance depends upon dynamic switching between the exsolved RuFe alloy NPs and dispersive Ru sites on SFRuM.

Discussion

In situ microscopy and spectroscopy characterizations reveal dynamic exsolution and dissolution processes of RuFe alloy NPs on SFRuM surface at the atomic scale, as well as Ru enrichment on SFRuM surface upon multiple exsolution and dissolution of Ru and Fe after repeated redox manipulations, which significantly promotes the exsolution of abundant RuFe alloy NPs on SFRuM surface. The density of exsolved RuFe alloy NPs reaches $\sim 21,000$ particles μm^{-2} after four redox manipulations, which is ~ 3.6 times as much as that after the first reduction treatment while the size of RuFe alloy NPs maintains similar. The in situ grown RuFe@SFRuM interfaces show highly active and stable electrochemical performance for CO_2 electrolysis in SOEC, as supported by EIS analysis and DFT calculations. Our study provides a strategy to obtain abundant catalytically active metal/oxide interfaces on perovskites for CO_2 electrolysis in SOEC and other heterogeneous catalytic reactions via repeated redox manipulations.

Methods

Chemicals. $\text{Sr}(\text{NO}_3)_2$ (AR, Aladdin Industrial Corporation), $\text{Fe}(\text{NO}_3)_3 \cdot 9\text{H}_2\text{O}$ (AR, Aladdin Industrial Corporation), $(\text{NH}_4)_6\text{Mo}_7\text{O}_{24} \cdot 4\text{H}_2\text{O}$ (AR, Sinopharm Chemical Reagent), RuCl_3 (AR, Tianjin Jinbolan Fine Chemical), glycine (AR, Sinopharm Chemical Reagent), citric acid monohydrate (AR, Sinopharm Chemical Reagent),

and polyvinyl alcohol (PVA, AR, Sinopharm Chemical Reagent) were used without any further purification.

Preparation of SFRuM perovskite. The perovskite powders were synthesized by a modified sol-gel method. For the synthesis of 0.03 mol (~12 g) of each perovskite, citric acid (15.0 g) and PVA (15.0 g) were added gradually in hot deionized water (70 °C, ~300 mL), metal precursors in the stoichiometric ratio were then dissolved to the above suspension and a clear solution precursor was obtained after concentration. A fluffy powder was obtained after the mild combustion on the heating plate, which was then calcined at 1100 °C for 10 h to obtain pure perovskite powder.

Characterizations. In situ and ex situ XRD measurements were performed on PANalytical Empyrean diffractometer (Cu K α radiation, $\lambda = 1.5432 \text{ \AA}$), and the spectra were collected in 2θ range of 20–80° at a scanning rate of 10° min⁻¹. Rietveld refinement was performed using GSAS software, and the data were recorded in 2θ range of 10–110° with a scanning rate of 2° min⁻¹. For in situ XRD measurements, the as-prepared SFRuM was initially heated to 800 °C, which was exposed to 50% H₂/Ar (100 mL min⁻¹) after Ar (50 mL min⁻¹) purging to investigate the reduction process. The reoxidation process was conducted in the air after Ar (50 mL min⁻¹) purging. This procedure was repeated twice under the same conditions.

XPS measurements were conducted with a spectrometer (PHOIBOS-100 analyzer from SPECS) equipped with an Al K α X-ray source operated at 300 W. Sample preparation: ~300 mg perovskite powders were calcined in 5% H₂/Ar (50 mL min⁻¹) or air (50 mL min⁻¹) in a tubular furnace at 800 °C for 2 h. A few milligrams of the reduced or reoxidized powders were collected during each process, which were pressed on the copper foam and transferred to the analysis chamber immediately.

In situ STEM measurements were performed on a HITACHI HF5000 (Environmental aberration-corrected TEM/STEM/SE) based on a standard 200 kV cold-field emission gun TEM, equipped with a highly sensitive secondary electron detector. Based on the surface and structural information from the SE, BF, and DF-STEM images, we can obtain a direct geometrical structure and acquire a deep understanding of the behavior under redox manipulations. In situ reduction and reoxidation of SFRuM were performed at 600–850 °C in 10 Pa H₂ and O₂ (2 mL min⁻¹). In situ STEM-EDS elemental maps and STEM-EELS could be obtained simultaneously. Ex situ atomic-scale crystal structure and STEM-EDS elemental maps were also obtained using this instrument, and the specimen was prepared with Leica EM UC7 microtome.

Ex situ STEM-EDS elemental maps were also collected on JEOL JEM F200. SEM images were obtained on JSM-7800F. Raman spectrum was collected on a LabRAM HR 800 Raman spectrometer.

Electrochemical measurements. SOEC with a configuration of SFRuM-GDC | LDC (La_{0.4}Ce_{0.6}O_{2- δ})|LSGM (fuel cell materials)|BSCF (Ba_{0.5}Sr_{0.5}Co_{0.8}Fe_{0.2}O_{3- δ})-GDC was fabricated. LSGM electrolyte was fabricated by dry-pressing LSGM powder under 200 MPa and then treated at 1450 °C for 10 h in air. The electrolyte pellet was ~500 μm thick and ~20 mm in diameter. BSCF was synthesized by a sol-gel method³¹. LDC and GDC fluorite phase powders were synthesized by a glycine combustion method⁵². The obtained LDC powder was mixed with viscid gum consisting of *a*-terpineol (Alfa Aesar), ethyl cellulose (SECOMA), and S-2800 (Shanghai Kaikai Chemical) with a mass ratio of 24:67:5:4 to prepare an LDC slurry by ultrasonic dispersion, which was spin-coated onto one side of the LSGM electrolyte and calcined at 1200 °C for 3 h to obtain LDC interlayer. SFRuM-GDC (60:40 wt%) composite cathode was assembled on the surface of the LDC side and BSCF-GDC (50:50 wt%) composite anode was assembled on the opposite side with an active area of 0.5 cm², followed with treatment at 1100 °C for 2 h. CO₂ electrolysis performance was measured on a homemade device⁵². Au paste was used as the current collector. The reduction and reoxidation processes of the cathode were conducted under 5% H₂/Ar (20 mL min⁻¹) and air (20 mL min⁻¹) at 800 °C, respectively. 95% CO₂ + 5% N₂ was fed to the cathode (50 mL min⁻¹, N₂ as internal standard gas) and the products were detected by online gas chromatography (Agilent GC490). The measurements at different voltages were conducted using Metrohm Autolab potentiostat/galvanostat (PGSTAT 302 N). I–V curves were recorded from 0.3 to 1.6 V by a sequential step change of 10 mV s⁻¹. EIS was recorded in a frequency range of 1 MHz to 0.1 Hz under an amplitude of 10 mV.

Computational models and methods. Spin-polarized DFT calculations were implemented using a plane-wave basis set in the Vienna Ab-initio Simulation Packages (VASP 5.4)⁵³. The exchange-correlation energy was treated using Perdew–Burke–Ernzerhof (PBE)⁵⁴ functional within the generalized gradient approximation (GGA)⁵⁵. The projected-augmented wave (PAW)⁵⁶ pseudopotentials were utilized to describe the core electrons, and a cutoff energy of 400 eV was used for the plane-wave expansion. The following valence electron configurations were included in the self-consistent field calculations: Sr (4s², 4p⁶, and 5s²), Fe (3d⁶ and 4s²), Mo (4d⁵ and 5s¹), Ru (4d⁷ and 5s¹), O (2s² and 2p⁴), and C (2s² and 2p²). In addition, the van der Waals (vdW) dispersion forces were corrected by the vdW-DF (optPBE) function, which showed a highly accurate description for oxides⁵⁷. An on-site Hubbard term U–J was added to address the open-shell *d*-electrons (2.89 eV

for Fe)⁵⁷. The energies and residual forces were converged to 10⁻⁶ eV and 0.01 eV \AA^{-1} , respectively.

Models. According to the characterizations by XRD and TEM in Supplementary Fig. 1, the crystal structures are referenced to SFM (Sr₂Fe_{1.5}Mo_{0.5}O_{6- δ}) (*Pnma*, no. 62) before reduction and RP-SFM (Sr₃FeMoO_{7- δ}) (*I4/mmm*, no. 139) after reduction. The optimal lattice constants are $a = c = 5.50 \text{ \AA}$ and $b = 8.00 \text{ \AA}$ for a ferromagnetic (FiM) Sr₄Fe₃MoO₁₂ (SFM) cell, and $a = b = 3.93 \text{ \AA}$ and $c = 20.84 \text{ \AA}$ for a FiM Sr₆Fe₃MoO₁₄ (RP-SFM) cell (Supplementary Fig. 32)³¹. Accordingly, a Sr₁₈Fe₈Mo₄O₄₂ supercell was adopted to warrant the stoichiometry ratio of Fe:Mo = 2:1. Here, we referred to SFM and RP-SFM as SFRuM and RP-SFRuM with consideration of only trace Ru in bulk. For structural evolution, the SFRuM[010] orientation is considered to explain the segregation ability of B-site dopants with or without oxygen vacancy and/or exsolved Ru. A slab with four Fe-O and three Sr-O layers was utilized to mimic the SFRuM(010) facet, where the bottom two layers were constrained. To evaluate the catalytic performance, the SFRuM(121) facet were used to model the pristine surface, where three Sr-Fe-O layers was included with the bottom two fixed (Supplementary Fig. 33a). And a simplified RP-SFRuM(105) ribbon integrated with a Fe₃Ru₃ cluster was utilized to simulate the interface structure, whose bottom two layers were constrained (RuFe@SFRuM, Supplementary Fig. 33b, c). For irreducible Brillouin zone sampling, a Monkhorst-Pack⁵⁸ k-point grid of 4 × 4 × 4 was adopted for Sr₄Fe₃MoO₁₂, 6 × 6 × 1 for Sr₆Fe₃MoO₁₄, and 6 × 2 × 1 for Sr₁₈Fe₈Mo₄O₄₂. A gamma point was exploited for all the surface and interface models. Denser k-point grids were adopted for the PDOS calculation. The vacuum thickness was more than 12 \AA between slabs.

Thermodynamic corrections and formulae. Energy levels of the states were corrected to Gibbs free energies by the formula:

$$G(T) = E_{\text{elec}} + ZPE + \delta H - T\Delta S \quad (1)$$

Where E_{elec} is the electronic energy calculated by DFT at 0 K, ZPE is the zero-point energy, δH is the integral of heat capacity, and $T\Delta S$ is the energy of entropy change ($T = 800 \text{ °C}$). For adsorbed species, the last three items were obtained by vibrational frequencies calculations via standard methods⁵⁹. For gaseous species, the corrections were taken from the *NIST* database through standard ideal-gas methods⁶⁰. The relevant values are listed in Supplementary Table 4.

The exchange energy²⁸ (E_{exc}) and segregation energy^{14,35} (E_{seg}) of B-site metals (X) were defined as:

$$E_{\text{exc}} = E_{X_{\text{inL}}} - E_{X_{\text{3L}}} \quad (2)$$

$$E_{\text{seg}} = E_{(X)_{\text{surf}}} - E_{(X)_{\text{bulk}}} \quad (3)$$

Where $E_{X_{\text{inL}}}$ is the energy of locating X at the *n*-th layer away from the surface layer (the first layer is termed 1L, henceforth). The third layer (3L) is treated as the bulk location, which energy is $E_{X_{\text{3L}}}$ as the zero reference. $E_{(X)_{\text{surf}}}$ and $E_{(X)_{\text{bulk}}}$ are the total energies of the systems with X located at the surface and in the bulk, respectively. Here, a negative value means high stability.

The adsorption energy ($E_{\text{ads},\text{CO}_2}$) of CO₂ were calculated by:

$$E_{\text{ads},\text{CO}_2} = E_{\text{CO}_2^*} - E_* - E_{\text{CO}_2} \quad (4)$$

Where $E_{\text{CO}_2^*}$ is the energy of a CO₂ adsorbed on the site (*), E_* is the energy of a clean site, and E_{CO_2} is the energy of the gaseous CO₂.

The formation energy of oxygen vacancy (E_{ovf}) is defined as:

$$E_{\text{ovf}} = E_{V_{\text{O}}} + E_{\text{CO}_2} - E_{\text{int}} - E_{\text{CO}} \quad (5)$$

Where $E_{V_{\text{O}}}$ and E_{int} are the total energies of the oxygen-defected and the intact surfaces. E_{CO} is the energy of gaseous CO.

The electron density differences were calculated using the formula:

$$\Delta\rho = \rho_{\text{CO}_2^*(V_{\text{O}})} - \rho_{s(V_{\text{O}})} - \rho_{\text{CO}_2} \quad (6)$$

Data availability

The data that support the findings of this study are available from the corresponding author upon reasonable request due to the data are of large amount. Source data are provided with this paper.

Received: 15 March 2021; Accepted: 27 July 2021;

Published online: 27 September 2021

References

- Hauch, A. et al. Recent advances in solid oxide cell technology for electrolysis. *Science* **370**, 186 (2020).

- Ebbesen, S. D., Jensen, S. H., Hauch, A. & Mogensen, M. B. High temperature electrolysis in alkaline cells, solid proton conducting cells, and solid oxide cells. *Chem. Rev.* **114**, 10697–10734 (2014).
- Li, Y. et al. Controlling cation segregation in perovskite-based electrodes for high electro-catalytic activity and durability. *Chem. Soc. Rev.* **46**, 6345–6378 (2017).
- Song, Y. et al. High-temperature CO₂ electrolysis in solid oxide electrolysis cells: developments, challenges, and prospects. *Adv. Mater.* **31**, 1902033 (2019).
- Irvine, J. T. S. et al. Evolution of the electrochemical interface in high-temperature fuel cells and electrolyzers. *Nat. Energy* **1**, 15014 (2016).
- Zhang, J., Gao, M.-R. & Luo, J.-L. In situ exsolved metal nanoparticles: a smart approach for optimization of catalysts. *Chem. Mater.* **32**, 5424–5441 (2020).
- Kim, J. H. et al. Nanoparticle ex-solution for supported catalysts: materials design, mechanism and future perspectives. *ACS Nano* **15**, 81–110 (2020).
- Park, S. et al. In situ exsolved Co nanoparticles on Ruddlesden-Popper material as highly active catalyst for CO₂ electrolysis to CO. *Appl. Catal. B* **248**, 147–156 (2019).
- Park, S. et al. A sulfur-tolerant cathode catalyst fabricated with in situ exsolved CoNi alloy nanoparticles anchored on a Ruddlesden-Popper support for CO₂ electrolysis. *J. Mater. Chem. A* **8**, 138–148 (2020).
- Choi, J. et al. Highly efficient CO₂ electrolysis to CO on Ruddlesden-Popper perovskite oxide with in situ exsolved Fe nanoparticles. *J. Mater. Chem. A* **9**, 8740–8748 (2021).
- Nishihata, Y. et al. Self-regeneration of a Pd-perovskite catalyst for automotive emissions control. *Nature* **418**, 162–164 (2002).
- Tanaka, H. et al. Self-regenerating Rh- and Pt-based perovskite catalysts for automotive-emissions control. *Angew. Chem. Int. Ed.* **45**, 5998–6002 (2006).
- Ye, L. et al. Enhancing CO₂ electrolysis through synergistic control of non-stoichiometry and doping to tune cathode surface structures. *Nat. Commun.* **8**, 14785 (2017).
- Kwon, O. et al. Exsolution trends and co-segregation aspects of self-grown catalyst nanoparticles in perovskites. *Nat. Commun.* **8**, 15967 (2017).
- Duan, C. et al. Highly efficient reversible protonic ceramic electrochemical cells for power generation and fuel production. *Nat. Energy* **4**, 230–240 (2019).
- Zhu, Y. et al. Promotion of oxygen reduction by exsolved silver nanoparticles on a perovskite scaffold for low-temperature solid oxide fuel cells. *Nano Lett.* **16**, 512–518 (2016).
- Onn, T. M. et al. Smart Pd catalyst with improved thermal stability supported on high-surface-area LaFeO₃ prepared by atomic layer deposition. *J. Am. Chem. Soc.* **140**, 4841–4848 (2018).
- Neagu, D. et al. In situ growth of nanoparticles through control of non-stoichiometry. *Nat. Chem.* **5**, 916–923 (2013).
- Katz, M. B. et al. Reversible precipitation/dissolution of precious-metal clusters in perovskite-based catalyst materials: bulk versus surface redispersion. *J. Catal.* **293**, 145–148 (2012).
- Neagu, D. et al. Nano-socketed nickel particles with enhanced coking resistance grown in situ by redox exsolution. *Nat. Commun.* **6**, 8120 (2015).
- Katz, M. B. et al. Self-regeneration of Pd-LaFeO₃ catalysts: new insight from atomic-resolution electron microscopy. *J. Am. Chem. Soc.* **133**, 18090–18093 (2011).
- Myung, J. H., Neagu, D., Miller, D. N. & Irvine, J. T. S. Switching on electrocatalytic activity in solid oxide cells. *Nature* **537**, 528–531 (2016).
- Madsen, B. D. et al. Nucleation of nanometer-scale electrocatalyst particles in solid oxide fuel cell anodes. *J. Power Sources* **166**, 64–67 (2007).
- Sun, Y. F. et al. A-site-deficiency facilitated in situ growth of bimetallic Ni-Fe nano-alloys: a novel coking-tolerant fuel cell anode catalyst. *Nanoscale* **7**, 11173–11181 (2015).
- Han, H. et al. Lattice strain-enhanced exsolution of nanoparticles in thin films. *Nat. Commun.* **10**, 1471 (2019).
- Sun, Y. F. et al. New opportunity for in situ exsolution of metallic nanoparticles on perovskite parent. *Nano Lett.* **16**, 5303–5309 (2016).
- Kim, K. et al. Mechanistic insights into the phase transition and metal exsolution phenomena of Pr_{0.5}Ba_{0.5}Mn_{0.85}Co_{0.15}O_{3-δ} from simple to layered perovskite under reducing conditions and enhanced catalytic activity. *Energy Environ. Sci.* **14**, 873–882 (2021).
- Joo, S. et al. Cation-swapped homogeneous nanoparticles in perovskite oxides for high power density. *Nat. Commun.* **10**, 697 (2019).
- Joo, S. et al. Highly active dry methane reforming catalysts with boosted in situ grown Ni-Fe nanoparticles on perovskite via atomic layer deposition. *Sci. Adv.* **6**, eabb1573 (2020).
- Hamada, I. et al. A density functional theory study of self-regenerating catalysts LaFe_{1-x}M_xO_{3-y} (M = Pd, Rh, Pt). *J. Am. Chem. Soc.* **133**, 18506–18509 (2011).
- Lv, H. et al. In situ investigation of reversible exsolution/dissolution of CoFe alloy nanoparticles in a Co-doped Sr₂Fe_{1.5}Mo_{0.5}O_{6-δ} cathode for CO₂ electrolysis. *Adv. Mater.* **32**, 1906193 (2020).
- Beck, A. et al. The dynamics of overlayer formation on catalyst nanoparticles and strong metal-support interaction. *Nat. Commun.* **11**, 3220 (2020).
- Neagu, D. et al. In situ observation of nanoparticle exsolution from perovskite oxides: from atomic scale mechanistic insight to nanostructure tailoring. *ACS Nano* **13**, 12996–13005 (2019).
- Liu, K. et al. Strong metal-support interaction promoted scalable production of thermally stable single-atom catalysts. *Nat. Commun.* **11**, 1263 (2020).
- Kim, K. et al. Control of transition metal-oxygen bond strength boosts the redox ex-solution in a perovskite oxide surface. *Energy Environ. Sci.* **13**, 3404–3411 (2020).
- Duan, C. et al. Highly durable, coking and sulfur tolerant, fuel-flexible protonic ceramic fuel cells. *Nature* **557**, 217–222 (2018).
- Neagu, D. et al. Demonstration of chemistry at a point through restructuring and catalytic activation at anchored nanoparticles. *Nat. Commun.* **8**, 1855 (2017).
- Sun, Y.-F. et al. Bifunctional catalyst of core-shell nanoparticles socketed on oxygen-deficient layered perovskite for soot combustion: in situ observation of synergistic dual active sites. *ACS Catal.* **6**, 2710–2714 (2016).
- Li, Y. et al. A novel fuel electrode enabling direct CO₂ electrolysis with excellent and stable cell performance. *J. Mater. Chem. A* **5**, 20833–20842 (2017).
- Mao, X. et al. Epitaxial and strong support interactions between Pt and LaFeO₃ films stabilize Pt dispersion. *J. Am. Chem. Soc.* **142**, 10373–10382 (2020).
- Wang, W. et al. Enhanced carbon dioxide electrolysis at redox manipulated interfaces. *Nat. Commun.* **10**, 1550 (2019).
- Aitbekova, A. et al. Low-temperature restructuring of CeO₂-supported Ru nanoparticles determines selectivity in CO₂ catalytic reduction. *J. Am. Chem. Soc.* **140**, 13736–13745 (2018).
- Tao, F. & Salmeron, M. In situ studies of chemistry and structure of materials in reactive environments. *Science* **331**, 171–174 (2011).
- Tao, F. et al. Break-up of stepped platinum catalyst surfaces by high CO coverage. *Science* **327**, 850–853 (2010).
- Du, Z. et al. High-performance anode material Sr₂FeMo_{0.65}Ni_{0.35}O_{6-δ} with in situ exsolved nanoparticle catalyst. *ACS Nano* **10**, 8660–8669 (2016).
- Zhang, X. et al. Enhancing electrocatalytic CO₂ reduction in solid oxide electrolysis cell with Ce_{0.9}Mn_{0.1}O_{2-δ} nanoparticles-modified LSCM-GDC cathode. *J. Catal.* **359**, 8–16 (2018).
- Li, Y. et al. Perovskite oxyfluoride electrode enabling direct electrolyzing carbon dioxide with excellent electrochemical performances. *Adv. Energy Mater.* **9**, 1803156 (2019).
- Bian, L. et al. Electrochemical performance and stability of La_{0.5}Sr_{0.5}Fe_{0.9}Nb_{0.1}O_{3-δ} symmetric electrode for solid oxide fuel cells. *J. Power Sources* **399**, 398–405 (2018).
- Lv, H. et al. Atomic-scale insight into exsolution of CoFe alloy nanoparticles in La_{0.4}Sr_{0.6}Co_{0.2}Fe_{0.7}Mo_{0.1}O_{3-δ} with efficient CO₂ electrolysis. *Angew. Chem. Int. Ed.* **59**, 15968–15973 (2020).
- Zhou, Y. et al. Pd single site-anchored perovskite cathode for CO₂ electrolysis in solid oxide electrolysis cells. *Nano Energy* **71**, 104598 (2020).
- Nørskov, J. K. et al. The nature of the active site in heterogeneous metal catalysis. *Chem. Soc. Rev.* **37**, 2163–2171 (2008).
- Lv, H. et al. In situ exsolved FeNi₃ nanoparticles on nickel doped Sr₂Fe_{1.5}Mo_{0.5}O_{6-δ} perovskite for efficient electrochemical CO₂ reduction reaction. *J. Mater. Chem. A* **7**, 11967–11975 (2019).
- Kresse, G. & Hafner, J. Ab initio molecular dynamics for liquid metals. *Phys. Rev. B Condens Matter* **47**, 558–561 (1993).
- Perdew, J. P., Burke, K. & Ernzerhof, M. Generalized gradient approximation made simple. *Phys. Rev. Lett.* **77**, 3865–3868 (1996).
- Perdew, J. P., Burke, K. & Wang, Y. Generalized gradient approximation for the exchange-correlation hole of a many-electron system. *Phys. Rev. B* **54**, 16533–16539 (1996).
- Kresse, G. & Joubert, D. From ultrasoft pseudopotentials to the projector augmented-wave method. *Phys. Rev. B* **59**, 1758–1775 (1999).
- Zeng, Z. et al. Towards first principles-based prediction of highly accurate electrochemical pourbaix diagrams. *J. Phys. Chem. C* **119**, 18177–18187 (2015).
- Monkhorst, H. J. & Pack, J. D. Special points for Brillouin-zone integrations. *Phys. Rev. B* **13**, 5188–5192 (1976).
- Peterson, A. A. et al. How copper catalyzes the electroreduction of carbon dioxide into hydrocarbon fuels. *Energy Environ. Sci.* **3**, 1311–1315 (2010).
- Chase, M. W. *NIST-JANAF Thermochemical Tables* 4th edn (American Institute of Physics, 1998).

Acknowledgements

We gratefully acknowledge financial support from the National Key R&D Program of China (Grant 2017YFA0700102), the National Natural Science Foundation of China (Grants 22125205, 22102175, 92015302, 22072146, and 21688102), Dalian National Laboratory for Clean Energy (DNL180404 and DNL201923), Dalian Institute of Chemical Physics (Grant DICP DMTO201702), Dalian Outstanding Young Scientist

Foundation (Grant 2017RJ03), and the Strategic Priority Research Program of the Chinese Academy of Sciences (Grant XDB17020200). G.X. Wang thanks the financial support from CAS Youth Innovation Promotion (Grant Y201938).

Author contributions

H.L. and G.W. designed and synthesized the materials, and conducted the electrochemical and structural characterizations. L.L. performed the theoretical calculation study. X.Z. and Y.S. performed the relaxation time distribution function and the experimental data analyses. H.M. and C.Z. performed in situ aberration-corrected STEM, STEM-EDS, STEM-EELS, and atomic-scale STEM analyses. N.T. performed ex situ STEM and STEM-EDS analyses. R.L. and Q.F. performed XPS analyses. H.L. and G.W. wrote and edited the manuscript with input from all authors. G.W. and X.B. designed and supervised the project. H.L. and L.L. contributed equally.

Competing interests

The authors declare no competing interests.

Additional information

Supplementary information The online version contains supplementary material available at <https://doi.org/10.1038/s41467-021-26001-8>.

Correspondence and requests for materials should be addressed to Guoxiong Wang.

Peer review information *Nature Communications* thanks Won Bae Kim and the other, anonymous, reviewers for their contribution to the peer review of this work. Peer reviewer reports are available.

Reprints and permission information is available at <http://www.nature.com/reprints>

Publisher's note Springer Nature remains neutral with regard to jurisdictional claims in published maps and institutional affiliations.



Open Access This article is licensed under a Creative Commons Attribution 4.0 International License, which permits use, sharing, adaptation, distribution and reproduction in any medium or format, as long as you give appropriate credit to the original author(s) and the source, provide a link to the Creative Commons license, and indicate if changes were made. The images or other third party material in this article are included in the article's Creative Commons license, unless indicated otherwise in a credit line to the material. If material is not included in the article's Creative Commons license and your intended use is not permitted by statutory regulation or exceeds the permitted use, you will need to obtain permission directly from the copyright holder. To view a copy of this license, visit <http://creativecommons.org/licenses/by/4.0/>.

© The Author(s) 2021